Hot target magnetron sputtering process: Effect of infrared radiation on the deposition of titanium and titanium oxide thin films

Robin Graillot-Vuillecot, Anne-Lise Thomann, Thomas Lecas, Christophe Cachoncinlle, Eric Millon, Amael Caillard

Hot target magnetron sputtering process: effect of infrared radiation on the deposition of titanium and titanium oxide thin films

Robin GRAILLOT-VUILECOT[1], Anne-Lise THOMANN[1], Thomas LECAS[1], Christophe CACHONCINLLE[1], Eric MILLON[1], Amaël CAILLARD[1]

[1] Groupe de Recherches sur l'Energétique des Milieux Ionisés (GREMI), UMR 7344, CNRS-Université d'Orléans, 14 rue d'Issoudun, Orléans cedex 2, France

Abstract: Titanium-based thin films are synthesized by the magnetron sputtering of a titanium target in pure argon or in a mixture of argon and oxygen (reactive regime) in three experimental configurations: a hot target configuration for which the target is thermally disconnected from the cooled magnetron body, a cold/conventional target configuration, and a cold target configuration with an additional infrared source introduced in the chamber to understand the role of the radiation on thin film properties. In hot configuration, the target temperature and its emissivity are measured and compared to a 0D steady state model taking into account the main different cooling mechanisms. IR radiations constitute the major part of the total energy deposited on the substrate during hot target magnetron sputtering, whereas an increase of target temperature allows a rise of sputtered Ti and Ti^+ species fluxes and slightly affect their kinetic energy. In reactive regime, the obtained films are constituted of polycrystalline anatase TiO_2, and an increase of target/IR source temperature leads to an improvement of crystallinity. In pure argon, hot configuration seems to enhance its porosity, induces columns exhibiting sharp-features, slightly modifies its crystalline properties and helps to decrease internal compressive stress.

Corresponding author. Amaël Caillard (amael.caillard@univ-orleans.fr)

Keywords: hot target; magnetron sputtering; titanium; infrared radiation.

1. Introduction

Magnetron sputtering and evaporation (vacuum, arc or electron beam based) are nowadays the most widely used physical vapour deposition (PVD) processes to eject atoms from a solid target allowing the formation of nanoparticles or thin films. In vacuum evaporation process [1], especially adapted for elements with low melting point, material is heated until atoms acquire enough energy to leave surface, and cross vacuum chamber with a very low energy (between 0.1 and 0.3 eV depending on the material) toward substrate. Deposition rate is very sensitive to the nature of materials, making thus difficult to evaporate high melting point elements and to obtain thin films of complex stoichiometry (polycationic oxides or alloys). In sputtering techniques, target is submitted to the bombardment of ions generated in a plasma or issued from an ion beam. This results in the ejection of energetic atoms (few 10's eV depending on sputtering conditions) that are able to form a dense thin film (compared to the thermal/vacuum evaporation technique), which can enhance the film hardness [2,3] but induces tensile or compressive intrinsic stress depending and the deposition conditions [4-6]. During sputter deposition, substrate is submitted to action of other energetic particles (ions, electrons, high-energy neutrals) that can transfer energy and thus affect film formation (sputtering, desorption, implantation, diffusion…) and morphology [7-10] In turn, film properties such as adhesion, stress, density, grain size, orientation and defects could be modified [11-14]. Even if magnetron sputtering techniques are widely used in industry, the synthesis of defect-free compounds containing labile (as fluor, lithium, sodium …) and low melting point (as gallium, indium ...) is a difficult task. Moreover, the synthesis of oxides and nitrides with appropriate stoichiometry, good crystalline quality at high deposition rate is really challenging [15-17]. This leads manufacturers to mix various deposition techniques and use post annealing treatments, which complicates the process and lowers its efficiency (in terms of energy saving and environmental fingerprint). A way to overcome these issues would be to perform sputtering of a hot target heated by ion bombardment, so emitting infrared (IR) radiations and acting as a substrate front heater. The effect of target radiation has been already observed almost 20 years ago [18]. But it was rather regarded as an undesired side effect. Whereas a cooling system is usually used to prevent the overheating of magnets and to limit the temperature of target in conventional sputtering configuration, it is possible to promote target surface heating by thermally disconnecting the rear side of target from cooled magnetron. This can even lead to a liquid target surface. Performing sputtering with a high target temperature leads to an increase of deposition rate [15-26], improves crystalline quality (especially oxides) and influences texture [19-26] without any-annealing

treatments, modifies stoichiometry, especially for thin film containing volatile/labile elements [27], enhances reactive sputtering stability by reducing hysteresis loop [28], enhances thin film hardness, decreases average surface roughness [24,25], allows heteroepitaxy framework film growth that usually requires high substrate temperature to overcome large lattice parameter mismatch between film and substrate [29]. This could also help igniting/sustaining magnetron discharge during the sputtering of a ferromagnetic target by reaching its target paramagnetic state above the Curie temperature [30-32]. This emerging technology could be very promising, but so far the temperature dependence of mechanisms related to material ejection (sputtering, evaporation), plasma properties (composition, energy distribution, density, …) and the mechanisms of film growth (under the effect of kinetic and radiative energy transfers) are not yet fully understood, and actually difficult to access and interpret. Moreover, the heating of target induced by ion bombardment cannot be adjusted and controlled properly regardless the plasma properties. The precise knowledge (and the control) of the target temperature is also experimentally challenging either by using thermocouples, thermopiles (heat flux sensor), pyrometers or by analysing thermal radiation spectrum using visible or near-IR spectrometer [33,34]. Modelling all the physical mechanisms occurring inside target/magnetron system (IR radiation loss, sputtering at high temperature, evaporation, enthalpy modification, heat propagation, residual cooling by conduction) and at surface (ion reflection, electron secondary emission, atom ejection …) to finally estimate target temperature is an interesting approach developed by different groups [34-38].

To explain the modification of thin film properties, two main energetic contributions can be pointed out. IR radiations emitted by hot target have been suspected by some authors [39] to play a key role (in the heating of growing film for example), but have never been quantified and clearly related to thin film quality. Second, high-energy species which are generally produced at target in conventional (cold) magnetron sputtering transfer their energy to growing film and modify its physical properties. The influence of target temperature on flux and on the energy of these species has never been measured even if research groups investigated the influence of hot target during sputtering [40,41] and pointed out the fact that this hot process should induce lower energy ejected species (due to evaporation mechanism).

The present paper aims at investigating both target temperature in hot configuration using a straightforward steady state model validated by experimental measurements and the effect of high target temperature on the sputtering process on the properties of titanium-based thin films (morphology, composition and structure) in pure Ar and in an Ar/O_2 gas mixture. As model material in research (largely documented in the literature) and

for various applications, titanium is a good candidate for this study. Especially the relative influence of IR radiations (emitted by the target) and the energy of condensing species (only Ti atoms and Ti^+ ions, here) on film properties are studied.

2. Experimental

2.1. Sputtering apparatus

Experiments were performed in a 6-way cross-shaped HV deposition chamber pumped down to 8.10^{-5} Pa using a 500 l/s turbomolecular pump. The pressure is regulated to 1 Pa during deposition with 20 sccm Ar flow rate, whereas the O_2 one is fixed to 0 for non-reactive sputtering (in metallic regime) and 2 sccm (50W) or 3 sccm (100 and 150 W) for reactive sputtering (in compound/oxide regime). The Ti target (thickness of 3 mm and a radius R of 25.4 mm) without (cold configuration) or with (hot configuration) a 1.8 mm thick MACOR® 2 inches ceramic disk, is clamped on magnetron (2 inches TORUS® from K.J. Lesker) backing plate. This ceramic disk thermally disconnects the target and promotes its temperature rise. However, clamping surrounding target to ensure electrical connection between magnetron and target induces a residual cooling. The magnetron is powered by a DC power supply (Pinnacle plus 5 kW) between 50 and 200 W in this study. A bichromatic pyrometer (IGAR 6 from Lumasense) placed outside vacuum chamber in front of a ZnSe viewport is used to measure target surface temperature (using the Wien law) and emissivity, denoted ε_{pyro}. The distance between ZnSe viewport and target is sufficient (about 300 mm) to neglect deposition on viewport and the modification of its transmission. The pyrometer is placed at the focusable position of 350 mm from the target in normal incidence and the spot size on the target is close to 3 mm. This emissivity naturally depends on the chemical properties of the target surface (metallic, partially or fully oxidized, roughness etc.) but also on the emitted angle Θ, the temperature T and the wavelength λ. In this study, ε_{pyro} is defined as the emissivity in the direction of the pyrometer (normal to the target surface, $\Theta = 0°$) in the 2-2.5 µm wavelength range at a temperature T and is a quasi-monochromatic directional emissivity. The precision of the measured temperature is estimated to 2%. Figure 1a displays the experimental set up during the deposition of thin films or during the measurement of the target temperature. During the cooling step of the target, the temperature measured with the pyrometer displays an inflection point corresponding to Ti solid state transition (β -Ti transforms into α -Ti below 882°C) as previously reported by Tesař et al [42]. This transition temperature is used to calibrate

directional emissivity ratio between both spectral ranges (1.5-1.6 and 2-2.5 µm) in pure Ar gas, which is found to be between 1.28 and 1.35. These values indicate that the emissivity decreases when wavelength increases, which is commonly observed for metals [43] and Ti in particular [44]. A mean value of 1.3 will be considered in this study. In hot configuration, target temperature reaches 660, 870 and 1010°C (± 50°C, high uncertainty between runs of experiments due to the progressive erosion of target, see after) for the 3 respective power values (50, 100 and 150 W) in pure Ar gas. These temperature values are measured in racetrack area (defined by r=13 mm) and thus are higher than temperature averaged on the whole surface area. The upper temperature, 1010 °C, is largely inferior to titanium melting temperature at 1 atm (1668°C). A thermocouple placed on rear side of Si sample indicates a rise of its temperature up to values ranging from 120 to 220°C in hot configuration depending on DC power, whereas temperature inferior to 50°C are obtained in cold configuration. A higher temperature on the front side of substrate is probable considering that silicon is a good thermal insulator.

The substrate holder is placed in front of target with a substrate/target distance of 45 mm and an angle of 45° as shown on Figure 1a. A heating source (covered by a titanium thick film) is installed in front of substrate holder in order to mimic (at the best) target IR radiation emission with the same distance and angle (see Figure 1a). Its temperature can be regulated between 20 and 800°C, but only two temperatures have been tested in this study (600 and 800°C). The addition of this heating source allows to work in three different deposition configurations: hot target, cold target and cold target assisted by IR radiation.

2.2. In-situ / in-operando analysis

As shown on Figure 1b, substrate holder can be removed and replaced by a 6 mm in diameter thermopile sensor (also called heat flux sensor, HFM) [45]. This latter is covered by a zynolite back paint and a copper disk (6 mm in diameter and 100 µm in thickness) is fixed on it using a thermal conductive paste. Due to the presence of cold junctions (whose temperature is fixed to 5°C) just below the active junctions of sensor, the thermopile acts as a bolometer and directly gives the value of heat flux arriving to sensor (based on Seebeck effect) expressed in mW/cm². All the energy of species impacting to the surface of sensor is converted into heat flux and so such system allows to measure the energy flux density (Φ) coming from gas conduction/convection (Φ_{gas}, neglected in this study), the plasma species (Φ_{plasma}) and IR radiations emitted by the hot parts of chamber, especially the target ($\Phi_{IR,target}$). A more detailed list of energy contributions will be given in the results section. In this Figure 1b, surface sensor is perpendicular to the glowing target surface (denoted $\perp$ geometry), but the sensor has also been placed parallel to the target (// geometry) as indicated by dashed blue arrow. Sensor

has been previously calibrated under vacuum according to the NIST protocol and using a homemade blackbody (ensuring absorption and emission coefficients close to 1) [45]. In our study, the black paint is covered by a copper disk and a Ti based thin film (10 min deposition time in pure Ar), so the sensor system cannot be considered as a blackbody anymore. A part of energy is reflected at thin film surface and must be taken into account. The reflected and absorbed parts of energy are difficult to precisely estimate. Considering emitting source as diffuse grey-body, we can estimate its steady-state temperature using the Stefan-Boltzmann law from the IR radiation (emitted by the hot target $\Phi_{IR,target}$ or the IR source $\Phi_{IR,sourcet}$ and expressed in mW/cm²) collected on sensor. Moreover, we consider that sensor temperature is much smaller than the emitting source one.

$$\Phi_{IR\,(x)}(\mathrm{T}) = \mathrm{A}\sigma\, T^4 \text{ with } A = \alpha\, \varepsilon\, \mathrm{F}_x\, \frac{\mathrm{S}}{S_{HFM}} \quad (1)$$

where σ is the Stefan-Boltzmann constant (5.67 10^{-8} W/m².K), A is a constant (without dimension), ε is the total emissivity which corresponds to ratio between the excitance of material and that of a blackbody, both integrated on Θ, T and λ (Θ defined the angle from the normal to the target surface). ε is considered as the total emissivity even if sensor only measured radiation emitted in its direction Θ. α is the total absorptivity of the sensor surface and F_x is radiative view factor (geometrical factor taking into account that only a portion of target IR emission can be detected by sensor) with x indicates the corresponding geometry (x= //, ⊥, 45°). Using a ray-trace software and assuming that the spectral radiance of target is Lambertian, $F_{//}$ and $F_{\perp}$ have been found to be equal to 3.7 10^{-3} and 1.3 $10^{-3,}$ respectively. $F_{//}$ can also be deduced from the analytical expression given in [46]. For substrate (Figure 1a) positioned with an inclination of 45°, software gives a view factor $F_{45°}$ of 3.3 10^{-3}. We found that the ratio $F_{45°} / F_{//}$ is equal to 0.89 (superior to the expected cos(45°) value), whereas 2.5 is obtained for $F_{45°} / F_{\perp}$ ratio. This 0.89 factor (close to 1) indicates that measurement performed in // geometry gives a good estimation of the flux energy density incoming onto substrate.

According to the large thickness of disk (100 µm) covering the black paint, we consider that all un-reflected energy is absorbed, converted into heat and transferred to thermopile. In both regimes (oxide and metallic), copper disk is covered (before recording the measurement) by a Ti metallic thin film (containing residual oxygen) prior to the recording of experiment. The thickness of this thin film reaches few hundreds of nanometers in // or in 45° geometry. This thickness is high enough to consider Ti thin film as an IR transducer absorbing all IR radiation up to few µm [47, 48]. So the absorptivity of sensor surface is not equal to the copper

one but to the Ti thin film in 45° or // geometry. Considering the evolution of refractive index and of the extinction coefficient of titanium bulk in near IR between 1.5 and 2 µm wavelength, an absorptivity of 0.3-0.35 has been found for such Ti thin film (obtained from Openfilter software and from the Fresnel laws). However, the Ti thin film is not purely metallic and contains oxygen species which increased its global absorptivity. Previously experiments have shown that an absorptivity of 0.5 for such Ti thin film was a good approximation [49,50]. This is the value that we took in this study. During the recording of heat flux in oxide regime, an oxide thin film with a thickness inferior to 100 nm covers the previously deposited Ti metallic thin film but the absorptivity of sensor surface is not modified considering that such additional TiOx thin layer onto Ti, is transparent to IR radiation. In this study, the absorptivity α of the Ti thin film (acting as IR transducer) is close to its emissivity. Indeed, considering local thermodynamic equilibrium, most metal can be considered as a diffuse grey body (contrary to most non-conductive materials).

An EQP energy resolved mass spectrometer (Hiden Analytical, EQP1000) is used to estimate the amount and the energy of species interacting with the substrate. Only the energy of Ti sputtered atoms and of Ti^+ ions have been considered in this study. The 200 µm orifice is used and the EQP faces target center at a distance of 100 mm. The distribution of Ti atoms has been obtained after their ionisation (electron bombardment) in EQP internal ioniser (RGA configuration). During ionisation, the initial energy of Ti atoms are of course modified, but we assume that this modification is similar for all energy distributions taken into account that these distributions are close to each other. In the mass spectrometer, ioniser is surrounded by a cage biased to 3.0 V (in our experiments) giving energy to ions and ensuring their transport up to the detector, so 3.0 eV has been subtracted to the distributions. An auto-tune procedure has been performed in order to adjust the different internal parameters of EQP and to optimize signal intensity.

A quartz microbalance (8 mm in diameter, 6 MHz quartz covered by gold) is placed in front of the center of Ti target (at a 120 mm distance) using water cooled crystal holder in order to measure deposition rate through a STM-2 transducer (INFICON).

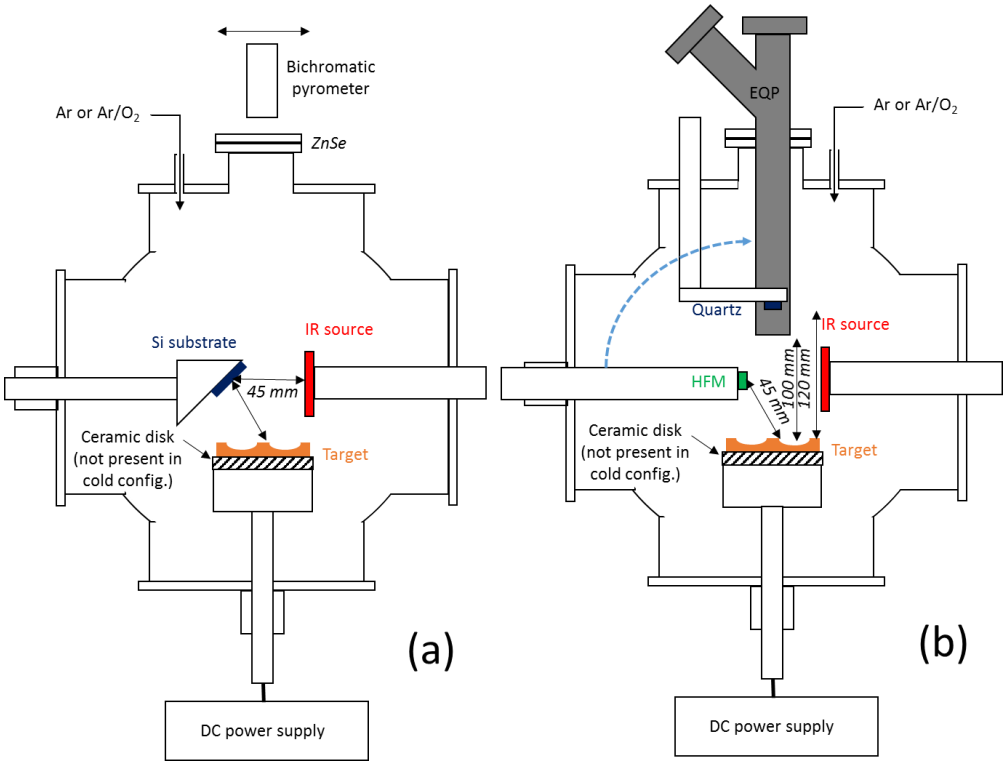

Figure 1. Experimental set up during deposition (a) or during in-situ diagnostic measurements (b) performed with heat flux microsensor (HFM) perpendicular to target surface (⊥ geometry), mass spectrometer (EQP), and quartz microbalance. The blue arrow indicates HFM is also placed parallel to magnetron (// geometry) at a 45 mm distance from target surface.

2.3. Ex-situ analysis

Eight metallic and eight oxide thin films were deposited on (100) Si substrates at three DC power values (50, 100 and 150 W) in cold configuration, with or without the presence of IR source, and in hot configuration as reported in Table 1. The samples are denoted *Ti_X_Y_Z* or *TiOx_X_Y_Z* (for metallic and reactive sputtering, respectively) where *X* stands for sputtering configuration (*cold* or *hot*), Y magnetron power and Z indicates if IR source was (or not) ignited and its corresponding temperature. Cathode voltage is reported for most conditions.

Rutherford backscattering spectroscopy (RBS) was used to compare the evolution of Ti and O amount in thin films deposited on Si substrates in the three configurations. The energy of probing ^{4}He particles and scattering angle were fixed to 2 MeV and 165°, respectively. Film cross-section (for morphology, and thickness analysis) was observed by scanning electron microscopy (SEM, Zeiss Supra 40). Structural characterizations were performed by X-ray diffraction in Bragg-Brentano geometry on a diffractometer (Bruker D8 Discover) using Cu Kα radiation (0.15406 nm). XRD patterns were compared to JCPDS files corresponding to anatase TiO_2

(00-021-1272 JCPDS files), rutile TiO_2, hexagonal α-Ti (00-044-1294) and cubic β-Ti (01-074-7075). Results obtained on the 16 thin films will be presented and discussed.

Table 1. Deposition conditions for the 16 thin films obtained in the 3 configurations in pure Ar and in Ar/O_2.

Name	Power (W)	Cathode voltage (V)*	Target temp. (°C)**	IR source temp.(°C)	Dep. time (min)
In pure Ar (metallic regime)					
Ti_Cold_50	50	270	<250	-	10
Ti_Cold_100	100	285	<250	-	10
Ti_Cold_150	150	-	<250	-	10
Ti_Cold_100_IR$_{600°C}$	100	295	<250	600	10
Ti_Cold_100_IR$_{800°C}$	100	295	<250	800	10
Ti_Hot_50	50	300	600	-	10
Ti_Hot_100	100	330	870	-	10
Ti_Hot_150	150	391	1010	-	10
In Ar/O_2 (oxide/reactive regime)					
TiOx_Cold_50	50	334	<250	-	180
TiOx_Cold_100	100	373	<250	-	80
TiOx_Cold_150	150	-	<250	-	80
TiOx_Cold_100_IR$_{600°C}$	200	369	<250	600	80
TiOx_Cold_100_IR$_{800°C}$	200	367	<250	800	80
TiOx_Hot_50	50	384	600	-	180
TiOx_Hot_100	100	422	800	-	80
TiOx_Hot_150	150	476	1000	-	80

* Voltage and power values correspond to the ones given by power supply.

** Temperature measured with bichromatic pyrometer focused on racetrack area (r=13 mm from target center).

3. Results and discussion

3.1. Target temperature evolution in hot configuration in metallic regime

This section focuses on the estimation of target temperature in hot configuration. First, a simple model based on energy balance at target is presented. Spatial distributions of the target surface temperature and directional emissivity are measured using bichromatic pyrometer. Last, mean target surface temperatures measured at steady state are compared to values calculated from model.

The control of process requires to precisely know target temperature as function of the power injected into the discharge. This is the reason why the measured temperature of target (T) is compared to values calculated from a 0D stationary model based on Bleykher et al [36-38]. This model takes into account all contributions: power

delivered on target by ion bombardment (W_{ion}), and power evacuated by heat radiation (W_{rad}), evaporation (W_{evap}) and sputtering processes (W_{sputt}), power due to the flux of reflected ions and to the gas convection being negligible. Target temperature is derived from the energy balance equation in stationary operation mode where W_{ion} W_{rad}, $W_{evap,}$ W_{sputt} represent the respective powers (expressed in W):

$$\boldsymbol{W_{ion} = W_{rad} + W_{evap} + W_{sputt}} \quad (2)$$

W_{ion} and W_{sputt} can be estimated as function of discharge parameters whereas W_{rad}, W_{evap} mainly depends on temperature, material emissivity, saturated vapour pressure, the specific heat of sublimation and the specific heat of condensed matter.

$$\boldsymbol{W_{ion} = S\, E_{ion}\, F_{ion} = P(1-\gamma)(1-\beta)} \quad (3)$$

Where S corresponds to target surface (πR^2 in cm^2), F_{ion} is the ion flux density impinging onto target (ion/cm^2/s), E_{ion} is mean energy of the ions (J/ion), γ is secondary electron emission (estimated to 5% here for titanium metal and for argon ion energies in the range of 200-500 eV [51,52]) and considered unchanged with temperature, $\boldsymbol{\beta}$ represents the energy loss of argon ions in cathodic sheath (estimated to 40% for an argon pressure of 1 Pa [37] and consistent with collisional plasma sheath model [53]). In our study, we consider a homogeneous ion flux over the whole target surface. But this is not the case in reality and the distribution of the current density should be taken into account in order to have a more precise calculation of the target temperature. P is the DC power delivered by power supply.

$$\boldsymbol{W_{rad} = S\, \varepsilon\, \sigma\, T^4} \quad (4)$$

Where ε is the total emissivity of target surface (integrated on all values of λ, Θ and T), σ is Stefan – Boltzmann constant. Losses at the rear side of target are neglected, we only consider the front side of the target (S).

$$\boldsymbol{W_{evap} = S\, F_{evap} \Delta H} \quad (5)$$

Where $\boldsymbol{F_{evap} = \sqrt{\frac{1}{2\pi mkT}}(P_{sat} - P')}$, $\boldsymbol{\Delta H = L_0 + \frac{3}{2}kT - c_pT}$ and $\boldsymbol{P_{sat} = exp(2.303(C - \frac{D}{T}))}$

Where F_{evap} is the flux density of metal atoms leaving target (at/m^2.s) according to Hertz-Knudsen law, $\boldsymbol{\Delta H}$ is the difference of enthalpy between the two phases (vapour and condensed state) (J/at), $\boldsymbol{\frac{3}{2}kT}$ is the mean energy of atoms leaving target (J/at) for monatomic gas, k is the Boltzmann constant, m is the mass of evaporated atom (kg), L_0 is standard heat of sublimation per atom ($7.23\ 10^{-19}$ J/at) at 0 K, c_p is the specific heat of condensed matter (in $4.3\ 10^{-29}$ J/at.K) close to 3k according to Dulong et Petit law, P_{sat} is saturated vapour

pressure at surface temperature T (Pa), P' is vapour pressure at target surface temperature T including the pressure of ejected metal and working gas (both neglected here compared to P_{sat}), the 2.303 multiplier is used to convert the base-10 logarithm to the natural one, C and D are metal coefficients determining the saturated vapor pressure of target material in the Hertz-Knudsen equation. Different values of these coefficients can be found in literature [54, 55]. In this study, mean values of 10 and 23000 have been taken for C and D, respectively.

$$\boldsymbol{W_{sputt} = S\, F_{sputt}\, E_{sputt} = S\, Y\, F_{ion} E_{sputt}} \quad (6)$$

Where $\boldsymbol{Y = \frac{3}{4\pi^2 U_S}(1-\alpha)U_s(0.15 + 0.13\frac{M_{Ti}}{M_{Ar}})(\frac{4M_{Ti}M_{Ar}}{(M_{Ti}+M_{Ar})^2})}$, $\boldsymbol{F_{ion} = \frac{Id}{qS}\,(1-\gamma)}$ and $\boldsymbol{E_{sputt} = U_s/2}$

Where F_{sputt} is the atomic flux density of sputtered atoms, E_{sputt} is the mean energy of sputtered atoms, Y is the sputtering yield, M_{Ti} is the molar weight of Ti atom, M_{Ar} is the molar weight of Ar atoms, I_d is the discharge current, U is the cathode voltage, I_d is the cathode current, U_s is the Ti binding energy (4.85 eV).

From equation (2), the temperature of Ti target can be estimated assuming that there are no conduction losses between target and magnetron (rear side and target area in contact to the clamping ring). Such conduction losses could induce a decrease of steady state temperature and eventually modify its uniformity (thermal gradient along the radius). In hot configuration, since thermal conduction is intentionally impeded at rear side, the first assumption sounds reasonable. On the contrary, it seems likely that thermal losses occur at clamping ring. Figure 2a displays the measured temperature of Ti target surface for 100 and 200 W (in pure Ar) along diameter (origin at target center). The temperature measured at target center is 860 °C for 100 W, and a temperature decrease of 150°C along a 8 mm distance is observed to target edge (corresponding to thermal gradient of 2 10^4 K/m). The mean temperature calculated on the whole circular surface is 788°C as reported on graph (dashed line). The temperature decrease is equal to 300°C for 200 W (thermal gradient of 4x10^4 K/m) with a temperature of 1130°C at center and a mean one of 1058°C. In the case of highly eroded targets, we have observed that temperature gradient between center and outer limits becomes higher due to the decrease of thermal conduction in the racetrack area. Thus, the temperature of target centre is higher for an used target than for a fresh one.

The directional emissivity in the 2-2.5 µm spectral range ε_{pyro} is reported on Figure 2b along target diameter in pure Ar. ε_{pyro} is minimum in the racetrack area between |6| and |16| mm and reaches minimum values of 0.14

at 200 W and 0.17 at 100 W, but largely increases in the outer limit of target to reach values above 0.3. A small dump (at 0.2 value) in the target is observed at center for 100W. These spatial evolutions of ε_{pyro} are due to differences in the physical state of target: very smooth surface in sputtered area, but rough and partly oxidized surface at center and around edge. The emissivity averaged over the whole target surface $<\varepsilon_{pyro}>$ (dashed lines on graph 2b) is found to decrease from 0.26 to 0.22 between 100 and 200 W, as reported on the graph. This could appear surprising at first glance (ε generally increases with temperature for metals [43]), but is related to the physical state of target that may not be the same, depending on sputtering power.

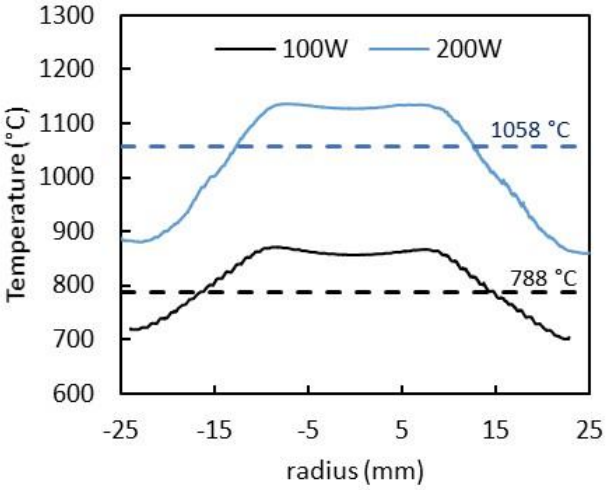

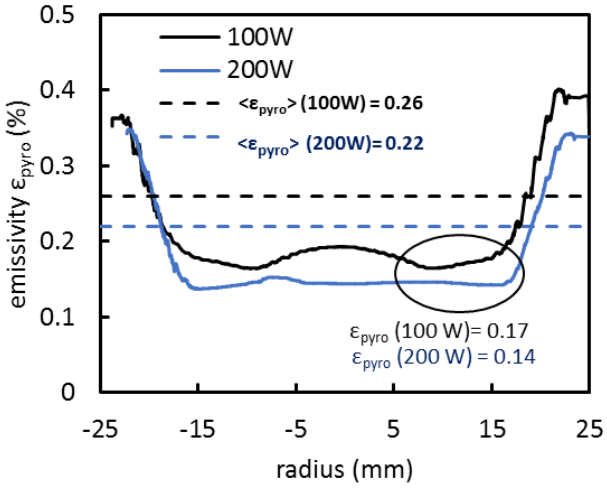

Figure 2. (a) Evolution of the target temperature and (b) emissivity ε_{pyro} measured using a bichromatic pyrometer along the target radius at two power values in metallic regime (pure argon). The dashed lines represent the mean value of temperature and of emissivity calculated on the whole circular target surface.

Figures 3a and 3b display the time evolution of the target temperature (in the racetrack area, r ∼ 13 mm). Figure 3a is obtained by progressively increasing (by steps) power between 50 and 115 W, whereas on Figure 3b power remains unchanged over time. It is clearly seen that when plasma is lighted on, or when power is increased, the target temperature rises until it reaches a steady state. For both figures, the steady state temperature evolution is extrapolated by using the empirical function $T(t)=T_{\infty}\left(1-e^{-t/\tau}\right)$ where the two fitted parameters are τ, a time constant depending on the emissivity and the specific heat of the target (in particular), and T_{∞}, the achieved steady state temperature, as displayed in dashed line on Figure 3a and 3b. The temperature evolution obtained with the model is reported on Figure 3c (for a total emissivity ε equal to 0.30, 0.38 and 0.40) and compared to the steady state mean temperature T measured with pyrometer. This mean temperature over the whole target has been evaluated considering a temperature decrease of 7±2% from the temperature measured at r ∼ 13 mm. This is the percentage that we observed when comparing Figure 2a and 3b. Figure 3c shows that model with ε = 0.38 and experimental temperature measured by pyrometer are in good accordance for power up to 100 W. This total emissivity value is higher than $<\varepsilon_{pyro}>$ value measured by the pyrometer (0.22 at 200 W and 0.26 at 100 W) which can be due to the angular and wavelength dependence of emissivity. This shows that target is not a real diffuse grey-body as we previously assume. But the difference can also come from the emission of IR radiation at the rear side of target which would modify equation (4) by increasing the real emitting surface and so decreasing ε value. For 150 and 200 W, the experimental temperatures are above the modelling curve obtained for ε = 0.38 which confirms that emissivity decreases when its temperature increases or when its surface roughness decreases (both parameters being connected to the power). In addition to the temperature, this model allows to quantify the contribution of each energy loss mechanism. For a power ranging from 50 to 200 W, the mean target temperature is inferior to 1100°C and the IR radiation power density W_{rad} represents 99% of the total incoming power density W_{in}.

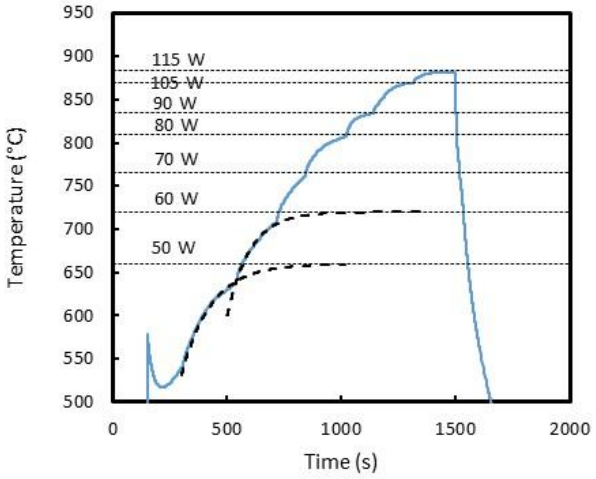

(a)

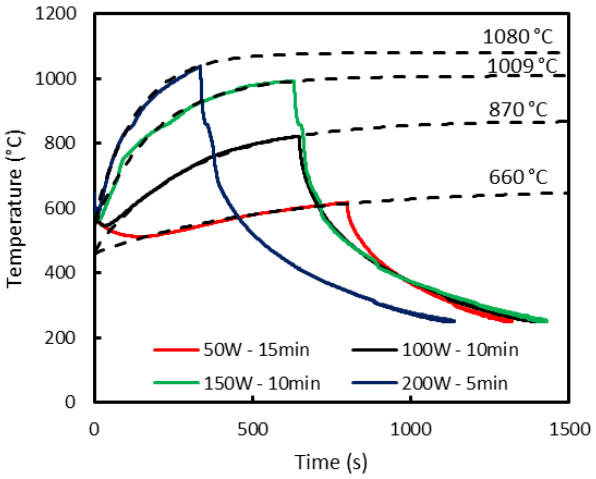

(b)

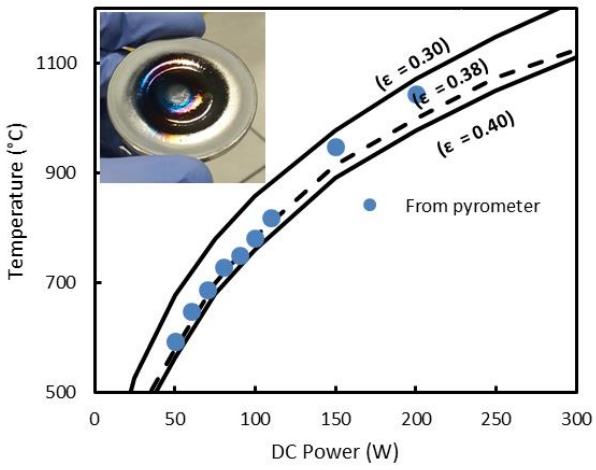

(c)

Figure 3. Time evolution of the Ti target temperature (in the racetrack area, r ~ 13 mm) for powers ranging from 50 to 200 W applied to cathode (a,b) and temperature evolution (in stationary mode and averaged on the whole target surface) as function of the power compared to modelling curves (for 3 ε values : 0.30, 0.38 and 0.40). A picture of the Ti target after sputtering under Ar/O_2 in hot configuration is added as inset in figure (c).

3.2. Effect of oxygen incorporation on the target temperature and emissivity

In reactive mode, O_2 introduction modifies the properties of target surface, its emissivity and so its cooling by radiation can drastically change. Figure 4 displays cathode voltage evolution, its temperature (in the racetrack) and its emissivity ε_{pyro} (in the 2-2.5 µm range) measured by the pyrometer facing the target at a DC power of 50 W for increasing and decreasing oxygen flow rates (0.1 sccm min^{-1}). Note that all temperature values and emissivities reported on this Figure are instantaneous measurements and do not correspond to steady state values for a given oxygen flow rate in steady state. The absolute value of voltage increases from 275 to 370 V when cathode goes through the metal/compound transition. Meantime, ε_{pyro} emissivity increases from 0.19 in pure argon at 50 W (which is slightly higher that the directional one obtained on Figure 2b at 100 W) to 0.30 corresponding to a 1.6 increased factor. Since oxides exhibit higher emissivity than metals, this trend was expected. At 100 W, pyrometer gives an emissivity of 0.17 in racetrack position whereas the total emissivity deduced from model is about 0.38 corresponding to a 2.2 increased factor. Consequently, the total emissivity in oxide regime is probably higher than 0.30. The spread between the way in and the way back result from the different dynamics of oxidation and thermal balance of the target, both processes evolving with its proper time constant. The minimum observed on the temperature curve around 1 sccm on way back, which corresponds strictly to the bump in emissivity at same flow, is interpreted as resulting from the very slow thermal response of target. Moreover, it is well-known that de-oxidation process does not occur in the same way than oxidation route, especially when competing with sputtering. Consequently, target surface state (oxidation degree, roughness etc.) at a given oxygen flow rate may not be the same on way in and back.

In addition, the target temperature and emissivity exhibit opposite trend. This is easily explained by the fact that reached temperature depends on the ability of target to be cooled by IR radiations, which is directly connected to the emissivity value. The target temperature decreases from 640°C to 580°C (by a 1.1 factor) when turning from metallic to oxide mode, whereas the emissivity increases from 0.19 to 0.30 (by a 1.6 factor). This indicates that the power released by radiation is rather constant ($1.1^4 \sim 1.5$) at 50 W.

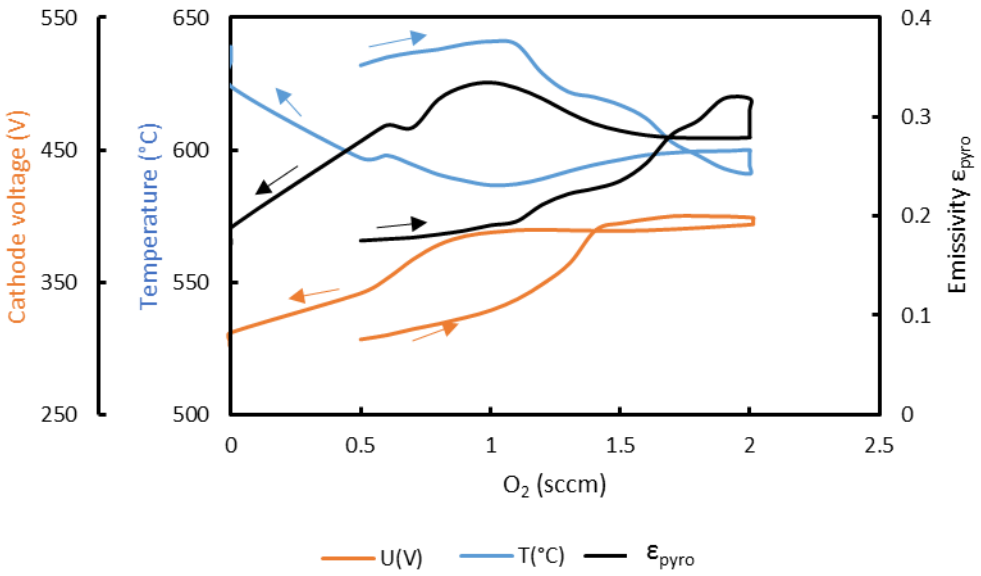

Figure 4. Target temperature, cathode voltage and emissivity ε_{pyro} as a function of the O_2 flow rate for 50 W.

The above results show how it is challenging to control target surface temperature in hot configuration. Actually, the obtained value at steady state is mainly determined by the absorbed power by target and its emissivity, which is spatially inhomogeneous and target-history dependent. Nevertheless, the experimental set-up developed in this work and the simple model used allows to get a good estimation of the target temperature.

3.3. Energy distributions of Ti atoms and Ti^+ ions by mass spectrometry

The energy distributions of Ti atoms and Ti^+ ions are measured and compared in hot/cold configuration on Figure 5 using mass spectrometry in pure argon. Only the distributions obtained at 150 W are presented. The maximum of the atomic distributions (a) is obtained for about 3.5 eV ($\sim$ 0.72 U_s) and seems to be unchanged between both configurations. Absolute intensity is increased in hot configuration, confirming the increase of deposition rate when target temperature rises. We do not observe any energy shift (to lower and higher value) or the appearance of Ti population group at low energy, which could have corresponded to evaporated atoms (3/2 kT = 0.15 eV for T=1150°C). Nevertheless, this does not rule out the existence of evaporation process since low intensity / low energy contributions may not be detected. Other techniques, as laser induced fluorescence, could be more relevant for this observation. As shown on Figure 5a, Thompson distribution largely overestimates the measured distribution for high energies due to collisions in gas phase at 1 Pa.

Stepanova et al [56] corrected this distribution by introducing a multiplicative factor ($1-E/E_{max}$). Both distributions on Figure 6a are well fitted by the Stepanova function with a cutting energy E_{max} of 25 eV for cold configuration and 20 eV for the hot one. The tail of both distributions at high energy can be also adjusted by a Maxwell-Boltzmann distribution with a kT constant of 4.5 and 4 eV for cold and hot configurations, respectively. These results show that a high target temperature slightly decreases the kT constant (or the cutting energy E_{max}) which leads to decrease the proportion of high energy sputtered atoms and so to a lower mean energy of the sputtered Ti species. This mean energy is equal to 6.9 eV for the distribution obtained in cold configuration and 6.35 eV for the one obtained in hot configuration. This decrease may be related to the decrease of the binding energy in materials when their temperature increases or other physical mechanisms as the ejection of clusters and the modification of cascade collisions process inside the materials. On Figure 5b, the Ti^+ ions energy distributions is composed of a low energy population between 0 and 4 eV and a high energy population up to 30 eV. As for the Ti distribution, absolute intensity is increased in hot regime, especially between 5 and 20 eV; but the amount of high energy ions seems to decrease in hot regime. The high energy tails are found to correspond to kT constant of 3 and 2.5 eV for respective cold and hot regime, which confirms the trend evidenced on Ti atom distributions.

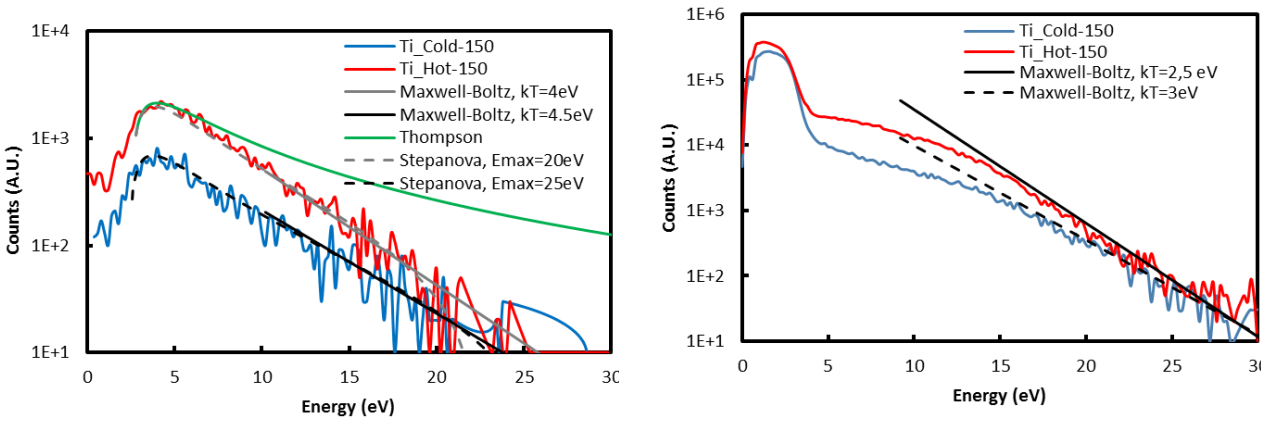

(a) (b)

Figure 5. Ti (a) and Ti^+ (b) energy distributions obtained using EQP mass spectrometer in cold (blue) and hot configuration (red) for metallic regime.

3.4. Energy flux density

The energy flux density measured by a thermopile sensor is given in Figure 6a for the *TiOx_Cold_150* (blue) and *TiOx_Hot_150* (red) deposition conditions with thermopile surface perpendicular to target surface (⊥ geometry). Between 0 and 750 s, plasma is running, but the shutter placed in front of target is closed. Thus, the increase observed is only due to IR radiation from the heated shutter (up to 35-70 mW/cm² at 750 s for the cold-hot configuration). When shutter is opened (750 s), a large increase of energy flux density is observed in both cases. These values reach about 70 and 190 mW/cm² for cold and hot target configuration (blue and red, respectively). These overall energies correspond to the sum of several energy contributions coming from:

(1) the kinetic energy of species sputtered and condensed on sensor and energy eventually released/absorbed during crystallization of these species or during surface chemical reactions.
(2) the kinetic energy of eventual species evaporated and condensed on sensor and energy eventually released/absorbed during the crystallization of these species or during surface chemical reactions.
(3) the conduction/convection energy coming from gas atoms (acting as cooling),
(4) the kinetic energy of high energy plasma species (neutralized and reflected species, negative and positive ions, secondary target electrons etc.)
(5) the eventual IR radiation emitted by the discharge
(6) the IR radiation emitted by all vacuum parts placed in front of the sensor and especially the target.

As already explained in previous studies [30, 39], the energy contribution corresponding to IR radiation can be measured by analysing the time recording of thermopile. When power is switched off (1321 s), all energy contributions coming from (1), (4) and (5) disappear in few ms and energy flux density quickly drops as shown on inset of Figure 6b. The (3) energy contribution measured just before starting the experiment (plasma off and experiment at room temperature) is equal to 8.2 mW//cm² in this work performed at 1 Pa [57] and we assume that this value is unchanged during the experiment. After subtracting this low value, the energy flux density measured just after plasma extinction (1321 s) results from the addition of the (2) contribution corresponding to the eventual evaporated species and the (6) contribution corresponding to the IR radiation emitted by the heated target (all other vacuum parts are much colder). But the (2) energy contribution can be neglected in the study since EQP measurements have shown that no significant low energy population has been detected at 150 W.

For indication, Figure 6b displays the "plasma contribution" in ⊥ geometry denoted $\Phi_{plasma\ (\perp)}$ (orange color) mainly corresponding to (4) energy contribution with the summation of the low (1) and (5) contributions. IR radiation arriving on surface sensor from target, denoted $\Phi_{IR,target\ (\perp)}$, and deduced by this procedure are shown on the graph (blue color). Finally, $\Phi_{plasma(\perp)}$ and $\Phi_{IR,target(\perp)}$ are respectively equal to 33 and 153 mW/cm² in hot target regime and 36 and 22 mW/cm² in cold target regime for these conditions (oxide regime, 150 W and ⊥ geometry). In hot target regime, this measurement reveals that the energy incoming onto the sensor is mainly due to the IR radiation emitted by target at 150 W in oxide regime, whereas $\Phi_{plasma(\perp)}$ represents a small part of total energy.

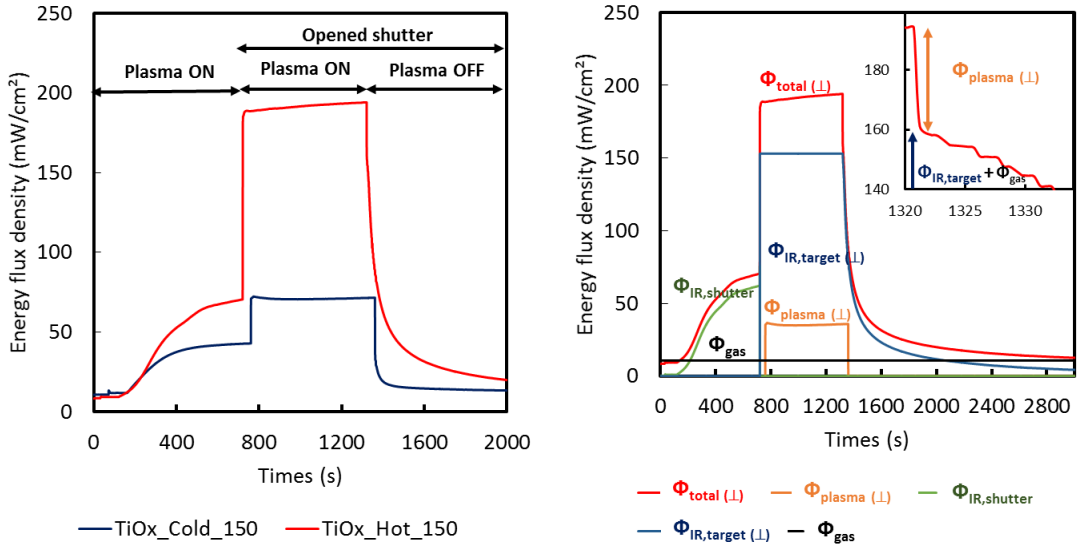

(a) (b)

Figure 6. (a) Energy flux density versus time in hot and cold configurations (with O_2, 150 W) for *TiOx_Hot/Cold_150*. (b) Overview of the different contributions of the energy flux density for the *TiOx_Hot_150*: IR radiations coming either from the shutter ($\Phi_{IR,shutter\ (\perp)}$) or from the target ($\Phi_{IR,target\ (\perp)}$), density coming from the gas (Φ_{gas}) and density coming from the energetic plasma species ($\Phi_{plasma\ (\perp)}$).

The measurement of energy flux density, $\Phi_{IR,target}$ and Φ_{plasma}, has been performed in all the conditions described in Table 1 with the HFM surface perpendicular to target surface (⊥ geometry) and for few conditions with the HFM surface parallel to target surface (// geometry). Figure 7a displays the density evolution of energy flux due to plasma species in ⊥ geometry, denoted $\Phi_{plasma\ (\perp)}$, as a function of the power applied to the cathode in pure Argon or in an Ar/O_2 mixture. $\Phi_{plasma,\perp}$ is proportional to the power delivered by the power supply from

0 to 150 W and the function expression is reported on the graph. The flux is 25% lower in oxide regime (light blue and orange symbols) than in metallic one (blue and red). In addition, hot configuration induces a small flux reduction of about 10% as compared to cold configuration in both cases (metallic and oxide regimes). This may be related to the decreased amount of high energy species (see EQP results) and to the production of low energy species.

Figure 7(b) and 7(c) shows the density evolution of the energy flux coming from the hot target $\Phi_{IR,target}$ or from the IR source $\Phi_{IR,source}$ as a function of target (or IR source) temperature in an Ar/O_2 gas mixture (b) or in pure Ar (c). To perform such measurements, HFM surface has been placed perpendicular and parallel to target or IR source surface (giving access to $\Phi_{IR,target\ (\perp)}$,$\Phi_{IR,target\ (//)}$$\Phi_{IR,\ source\ (\perp)}$ and $\Phi_{IR,source\ (//)}$). Experimental data are found proportional to the fourth power of temperature as expected from Stefan-Boltzmann law. Fitting curves described by the function $\Phi_{IR}(T)= \Phi_{IR,source}\ (T)= \Phi_{IR,\ target}\ (T)= A\sigma T^4$ are used on both figures for both geometries. The good agreement, which can be noticed between the absorbed IR radiations emanated from the hot target (red symbols) or the IR source (blue symbols), proves that this setup efficiently mimics the radiation coming from the hot target at a given temperature and will permit to isolate the effect of IR radiation on the substrate.

In // geometry, fitting curves are obtained with A equal to 0.045 and 0.075 for metal and oxide regime, respectively (where A is given by equation (1)). Considering an α absorptivity of 0.5 for sensor surface and a view factor of $3.4\ 10^{-3}$ in // geometry, a ε emissivity of 0.36 in metallic and 0.6 in oxide regime is deduced. Both emissivities are largely superior to the directional one measured by the bichromatic pyrometer but are consistent with the total one of target surface deduced from the model for metallic regime (0.38) and to the expected range in oxide regime. In $\perp$ geometries, A values obtained from the fitting curves (Figure 7b and 7c) is equal to $17\ 10^{-3}$ and $6.5\ 10^{-3}$ for metallic and oxide regime, respectively. If a value of 0.5 is used for absorptivity, a ε total emissivity of 0.36 in metallic is deduced, which is in accordance with the measurement performed in // geometry. In oxide regime, the thickness of the Ti film, deposited prior the TiO_x one, is too thin to guarantee that it acts as a good IR absorber and the copper absorptivity is much lower that the titanium

one. Indeed α is inferior to 0.1 for Cu in the 1-5 µm range using the Openfilter software based on refractive index and the extinction coefficient values from [58].

These measurements performed in both geometries give the upper and lower limits of energy flux density on the substrate in the deposition configuration (45° from the target surface). For metallic and oxide mode and assuming again that emission is Lambertian, the power density received on the substrate $\Phi_{ir,target\ (45°)}$ is obtained by multiplying the power density obtained in // geometry $\Phi_{ir,target\ (//)}$ by the $F_{45°}/F_{//}$ ratio (0.9). $\Phi_{ir,target\ (45°)}$ can also be obtained by multiplying the density obtained in ⊥ geometry $\Phi_{ir,target\ (\perp)}$ by the $F_{45°}/F_{\perp}$ (2.5) in metallic regime. Results is given in dashed line on Figure 7b and 7c. The comparison of graphs (a) and (b) confirmed that the energy flux density coming from the IR radiations emitted by the hot target is much higher than the one brought by plasma species in metallic conditions. For instance, at the substrate position (45°) and 100W corresponding to 870°C in metallic regime, the plasma contribution is around 75 mW/cm^2 and that of the IR radiation close to 400 mW/cm^2. At this power, 85% of the energy flux density arriving on the growing Ti thin film is due to IR radiation in metallic mode and this percentage increases with power/temperature. In oxide regime and for the same power, the plasma contribution is equal to 55 mW/cm^2 (22 x 2.5) and the IR radiation are also close to 400 mW/cm^2, which means that 88% of the energy flux density arriving on the growing TiO_x thin film is due to IR radiation in oxide mode. We must keep in mind that all these energy flux densities correspond to the absorbed part by sensor but not to the energy flux densities emanating from target.

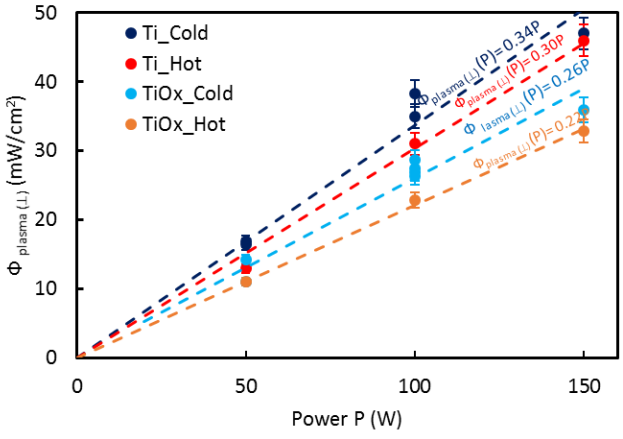

(a)

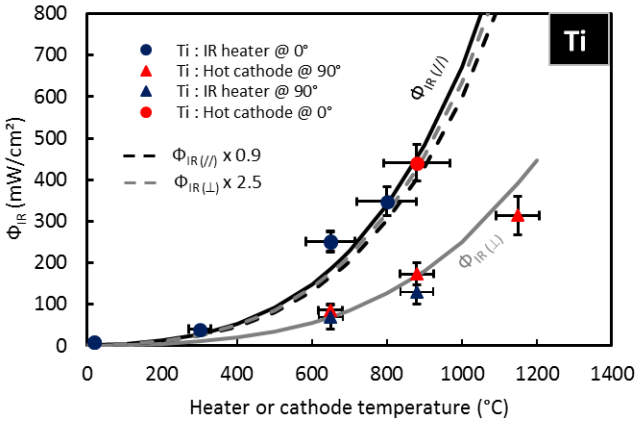

(b)

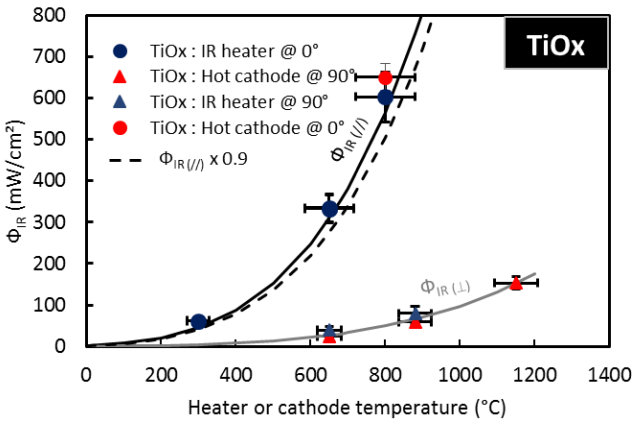

(c)

Figure 7. (a) Energy density flux $\Phi_{plasma\,(\perp)}$ as function of the power applied to the cathode and (b,c) energy flux density flux coming from the hot target or the IR source, in parallel (//) or in perpendicular geometry (⊥), and absorbed by the sensor surface as function of the target or heater temperature for (b) metallic and oxide (c) regime. Solid lines stand for Φ_{IR} estimated from the Stefan-Boltzmann law and dashed lines give the estimated values for the substrate position (angle of 45°).

3.5. Sputtering process and deposition rate

The thickness of each thin film has been measured on SEM images and the deposition rate, expressed in nm/min, has been calculated and reported in Figure 8 in pure Ar (a) and Ar/O_2 mixture (b) . These values (Δ symbols) are compared to the deposition rate obtained with quartz microbalance (o symbols). The deposition rate obtained using the microbalance, expressed in µg/min, are reported in nm/min on Figure 8a assuming a Ti density of 4.5 g/cm^3 and in µg/cm² on Figure 8b as TiO_x density is not known. In our setup, the quartz microbalance cannot be placed at the same location as the substrate during deposition (120 mm from target

instead of 45 mm in deposition configuration) and so the values of the deposition rates measured by microbalance and by SEM cannot be directly compared. However, the evolutions with respect of the DC power applied to the cathode and differences between metallic / oxide modes and cold / hot configurations can be discussed. Clearly, all the trends displayed in Figure 8 are in good agreement for both measurement techniques, which indicates that the density of films does not significantly evolve in the investigated ranges of parameters. In metallic mode and on the explored power range, the deposition rate linearly increases with rising power for cold and hot configuration in metallic mode and only for cold configuration in oxide mode. In this last case, in hot configuration, *d* exponentially rises (b, red marks). Such trends and behaviour in oxide have been already observed in literature and Musil et al [19] use two straight lines (representing the sputtering and the evaporation mechanisms) as fitting curves in oxide regime. Moreover, the values of deposition rate are found higher in the hot configuration than in the cold one. At 150 W, the deposition rates calculated from SEM cross sections reach 70 nm/min and 14 nm/min for respective metallic and oxide modes in hot configuration, whereas 50 and 7 nm/min are obtained in cold configuration. This corresponds to an increased factor of 1.4 and 2. This first value for metallic regime is relatively low compared to previous results obtained by Bleykher et al for Titanium [38], but the specific power was much higher in their study (up to 40 W/cm²) than one used here (up to 7.5 W/cm²). Both behaviours (enhanced deposition rate in hot configuration and higher increase in oxide regime) are not fully explained at that time. At such low specific power, evaporation mechanism is negligible according [40] and the EQP measurement supposing that low energy species are detectable. Our model indicates that the flux of evaporated atoms is 6 10^{14} at/cm².s, whereas the one of sputtered atoms is 10^{17} at/cm².s at 150 W (and 1010°C), as shown on Figure 8c. As sputtering is apparently the only ejection mechanism, this deposition rate increase could be related to a decrease of the binding energy or apparition/modification of other physical mechanisms. The addition of ceramic disk in hot configuration leads to an increase of the distance between the magnets and the target surface which modifies the discharge parameters (an increase of the cathode voltage in hot configuration is observed in Table 1 or for Ni in [30]) and may change the distribution of magnetic field lines. This can also be an explanation of the change of the deposition rate. Finally, the increase of deposition rate could also be related to the modification of sputtering yield between hexagonal α and cubic β Ti phases.

Finally, on Figure 8c is reported the deposition rate measured on SEM cross sections depending on the temperature of the additional IR source for metallic and oxide modes. The graph shows that the temperature

of IR source does not influence deposition rate without (blue) or with O_2 (orange). This result proves that IR radiations emitted by the cathode would certainly have no influence on condensation mechanism and that the enhancement of deposition rate in hot configuration (see Figure 8a and b) is rather due to a modification of atom ejection efficiency from hot target. A mean value of 45 nm/min is found for Ti thin film and 2.4 nm/min for TiO_x at 100 W. The lower value observed for TiO_x films (more than a ten factor) was expected and is typical of deposition carried out in oxide mode.

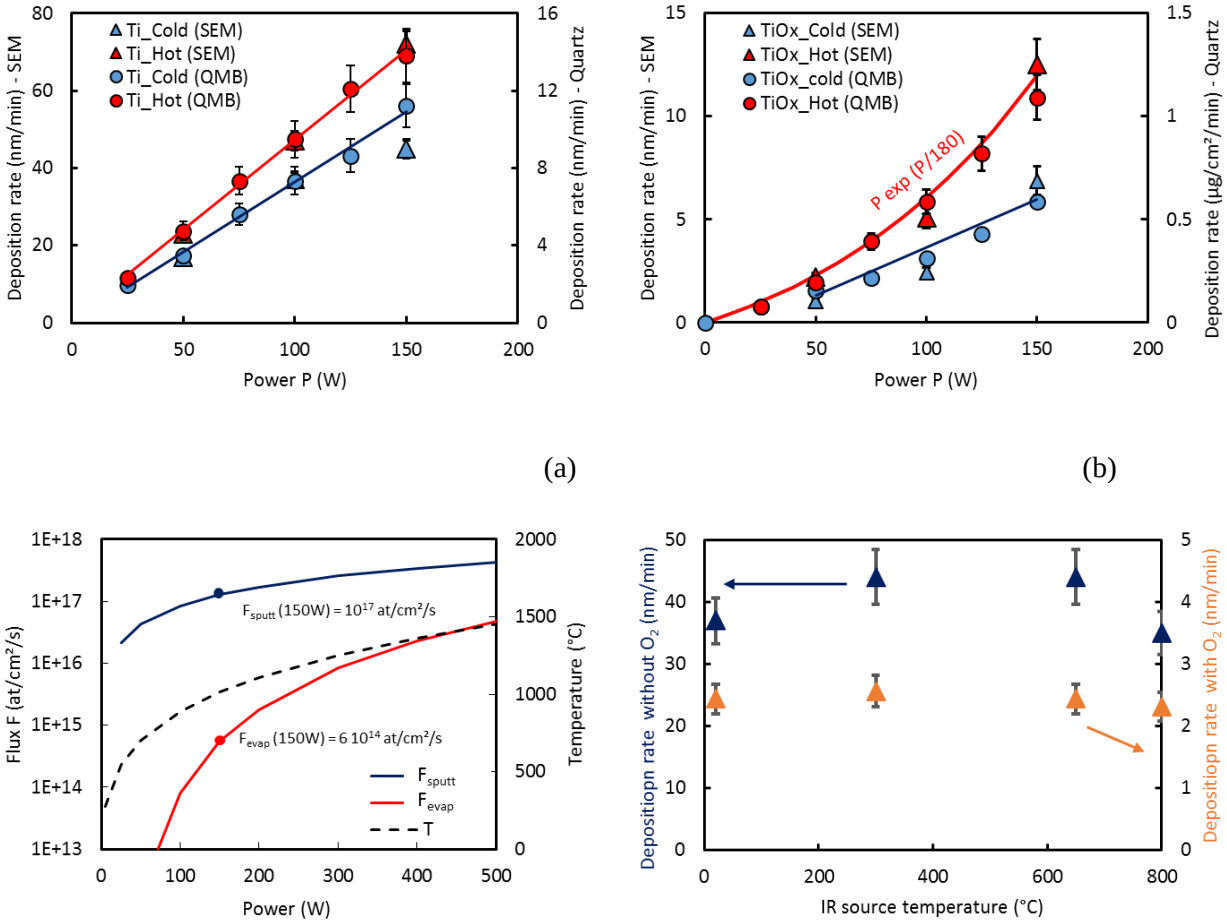

Figure 8. Deposition rate determined from SEM cross-section (Δ) and quartz microbalance (QMB) measurement (o) as function of the power applied to magnetron (a) without and (b) with O_2 in cold (blue) and hot (red) configuration. (c) Modelled sputtered F_{sputt} evaporated F_{evap} and target temperature as function of power. (d) SEM deposition rate in cold configuration as function of IR source temperature without oxygen (blue) and with oxygen (orange) at 100 W.

3.6. Morphology of thin films

Figure 9 compares the SEM cross section images corresponding to oxide thin films obtained in an Ar/O_2 gas mixture at 100 W in 3 configurations: cold (a), cold with IR (b) and hot (c). The images on Figures 9 c,d,e corresponds to the metallic thin films obtained in pure Ar in the same 3 configurations. These 6 thin films, whatever the configuration and the processing gas are, present a columnar morphology which is typical for thin film obtained by DC magnetron sputtering at this pressure (1 Pa) with tilted columns coming from the 45° deposition angle. No clear differences between the 6 first images are observed even if the structure appears more disordered (higher porosity, non-straight columns) in metallic thin films than in TiO_x ones. The hot configuration or the cold one with IR radiation does not modify thin film morphology for these deposition parameters and more specifically for 100 W. However, for higher power, here 150W, the morphology of the metallic thin film depends on the configuration as shown on Figures 9g) and 9h). *Ti_Hot_150* thin film (h) seems to display a more ordered structure (than that of all other deposits and notably the *Ti_Cold_150*) and its columns appear faceted and sharp-ended, whereas "smooth" ones are observed in the other deposition conditions. This change in column features from domed tops to sharp ends is typical of growth mode evolution from zone 1 to zone T [59,60] or zone 1a to zone 1c [61] according to the well-known structure zone models. This is usually related to an increase of the deposition temperature and is a proof that hot target configuration influences the mobility of adatoms on the surface.

However, this modification in the structure zone models generally goes with a thin film densification as it has been reported by Sidelev et al for chromium thin films [25,26,30] and a V-shaped column appearance. This is not the case here where thin film porosity seems to be enhanced in hot configuration. This higher porosity, typical of thin film obtained by vacuum evaporation, could be related to the decrease of the energy of condensing species evidenced by mass spectrometry even if evaporation mechanism can be neglected in our study taken into account the relative low specific power and low temperature.

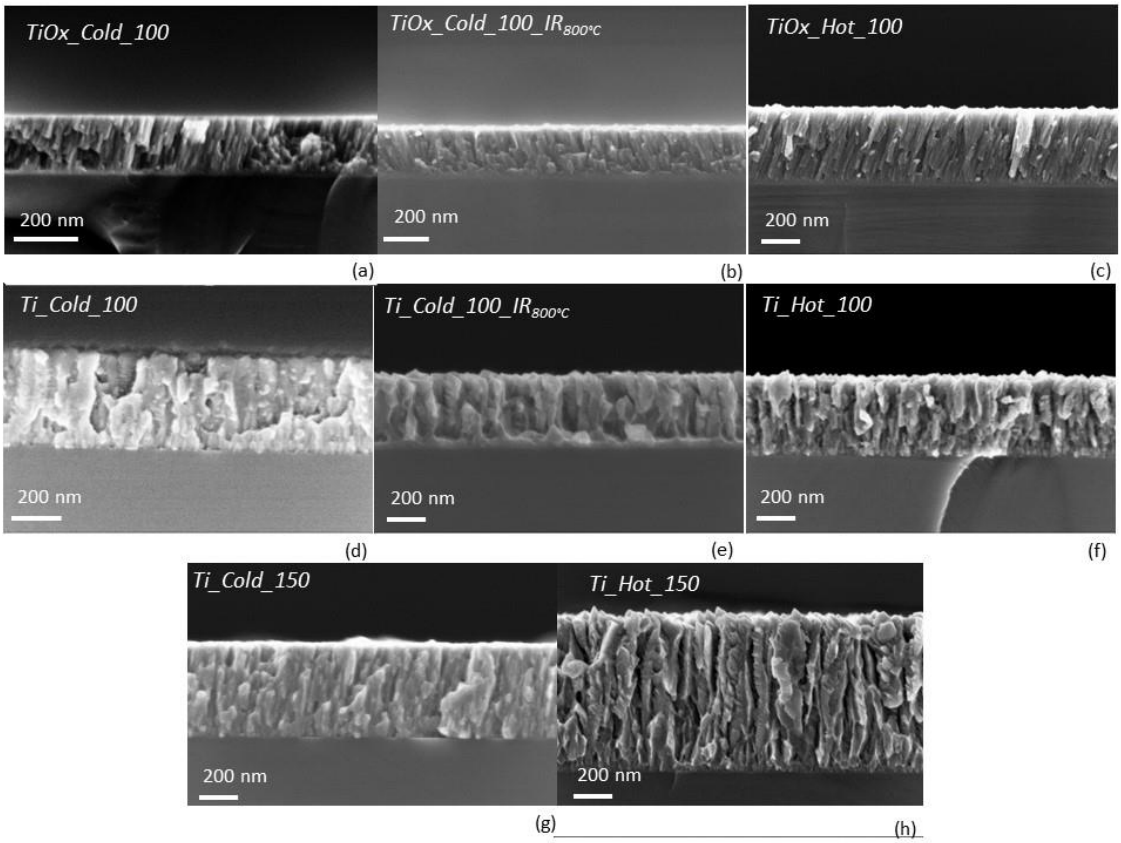

Figure 9. SEM cross section images corresponding to the 3 oxide thin films (*TiOx_Cold_100* (a), *TiOx_Cold_100*_$IR_{800°C}$ (b) and *TiOx_Hot_100* (c)), the 3 metallic thin films obtained for 100 W (T*i_Cold_100* (d), *Ti_Cold_100*_$IR_{800°C}$ (e) and *Ti_Hot_100* (f)) and the 2 metallic thin films obtained for 150 W (*Ti_Cold_150* (g) and *Ti_Hot_150 (h)*).

3.7. Oxygen content in films

Figure 10 displays the RBS spectra for titanium (a) and titanium oxide (b) thin films obtained at 100 W in the three configurations: hot (red), cold (blue) and cold with IR source (orange). On these graphs, the Ti peaks (between the 900^{th} and 1250^{th} channels) become larger in hot configuration (red) especially in Ar/O_2 mixture, whereas deposition time was unchanged. This confirms that larger thicknesses, and consequently deposition rates, are obtained in hot configuration, and that IR radiations do not impact condensation process. The small widening of the Ti peak observed in the case of cold configuration and IR source in metal mode (Figure 10b, orange curve) is not significant. On Figure 10a (TiO_x thin films), it can be seen that the maximum intensity of Ti peak decreases from 0.5 to 0.45 (as shown in the insert) when comparing the cold configuration to the two other configurations (hot and cold with presence of the IR source). This indicates that the deposition assisted by IR radiations (coming from the heated target or the IR source) enhances oxygen incorporation into thin

film. The O peak intensity (between the 300 and 700 channels) is not clearly modified but this is not surprising due to the low sensibility of RBS signal at low channels. On Figure 10b, the highest Ti peak corresponds to the thin film realized with IR source. If we assume, as suggested by the results obtained in Ar/O_2 mixture, that the incorporation of O is furthered in hot titanium, this trend can be explained. In pure Ar sputtering, residual oxygen is mainly consumed by the hottest surface in the vacuum experiment, i.e. the surface of the IR source that has been coated with Ti during previous runs of experiments. Additional IR source helps to consume residual oxygen into the chamber and so acts as an efficient O trapping device, in this case.

In order to obtain the absolute values of oxygen amount in these thin films, the spectra have been fitted using the Simnra® software, with Ziegler/Biersack stopping power data and Rutherford cross sections. In oxide mode, stoichiometric TiO_2 thin films are obtained in hot configuration or with the presence of the IR source, whereas in cold configuration under-stoichiometric thin films are synthesized (typically $TiO_{1.9}$). In pure Ar, when no oxygen is introduced in vacuum chamber, the oxygen percentage in the Ti- based thin film reaches large values: 25% in cold and hot configuration for 100 W. This high level of oxygen contamination inside Ti films is correlated to the very high affinity of this metal with oxygen. Of course, this percentage highly depends on the power applied on magnetron: 50% for 50 W, 25% for 100 W and 20% for 150W, since increasing the sputtered atom flux leads to higher Ti/O ratios inside films. As mentioned above, the addition of IR source allows to decrease percentage down to 15% for 100 W. All thin films obtained in pure argon are denoted "metallic Ti" film for convenience in the following section even if oxygen is present in these films.

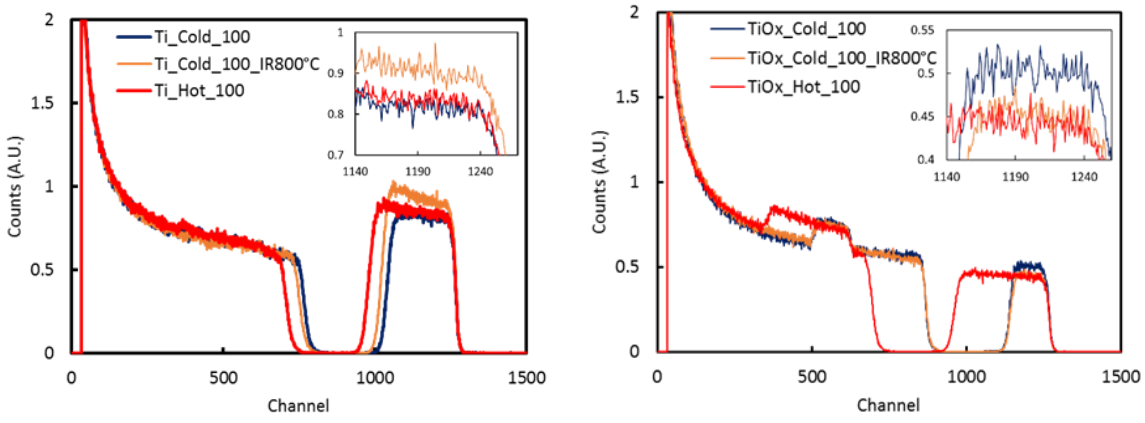

(a) (b)

Figure 10. RBS spectra for Ti (a) and TiO_x (b) thin films obtained in hot configuration (red), cold configuration (blue) and with the presence of the IR source (orange).

3.8. Structural properties of films.

3.8.1. Films obtained in oxide mode

By XRD, we have evidenced that the obtained TiO_x films are either amorphous or constituted by anatase TiO_2, no rutile or brookite phases being observed whatever deposition conditions. In literature, the stabilization of anatase or rutile phase during magnetron sputter deposition at low substrate temperature has been reported to widely depends on deposition conditions: total pressure, oxygen percentage in gas phase, target to substrate distance *etc*. [16,17,62]. Anatase phase is usually observed when energy transferred to the substrate during thin film growth is low [45]. In the present work, we focused our study on the comparison between cold and hot target configurations.

XRD analysis shows that all TiO_x thin films obtained at 50 W with a thickness of 400 nm are amorphous whatever the configuration. The diffractogram of *TiOx_Hot_50* film corresponding to a target temperature of 660°C is shown on Figure 11a. JCPDS data of tetragonal anatase TiO_2 (# 00-021-1272) are reported on Figure 11a (black dashed bars). When increasing power to 100W, the structure still remains amorphous as observed on the *TiOx_Cold_100* (Fig 11a in blue). At this power, IR radiation emitted by target or by IR source seems to promote crystallinity, since the (101) diffraction line of TiO_2 anatase phase is detected at 25.28°. By increasing power, the formation of polycrystalline tetragonal anatase phase is promoted as several peaks corresponding to the (004), (112), (200) (105) and (211) lattice planes are clearly visible on Figure 11a for the film obtained at 150W. However, this conclusion has to be handled with care, because the thickness of *TiOx_hot_150* is more than twice that of other samples. It is well established in magnetron sputtering technique that the crystallinity of a film is directly related to its thickness, reason why the study of effect of deposition conditions can only safely be performed on films of similar depth [61]. To overcome this issue, a second set of 3 deposits *TiOx_Cold_100*, *TiOx_Cold_100_IR* and *TiOx_hot_100* with the same thickness (1 µm) were performed by adjusting the deposition time (respectively fixed to 360, 360 and 180 min). Figure 11b gives the evolution of the main (101), (004), (112), (105) and (211) diffraction lines. The 3 films present a powder-like diffractogram of the TiO_2 anatase phase for which crystallites are randomly distributed on substrate; one can simply notice that the relative intensities of these 3 peaks are modified in hot target and cold + IR source configurations : the intensity of the (112) and (211) peaks is enhanced with the presence of IR radiation.

3.8.2. Films obtained in metallic mode

The XRD patterns of these films present the diffraction lines of hexagonal α-Ti phase (Figure 11c). The film obtained at the lowest power in cold configuration (*Ti_Cold_50)* is amorphous, while all other films exhibit diffraction lines corresponding to α-Ti bulk reference material (JCPDS #00-044-1294). Globally, same conclusions than before can be suggested: increasing power or adding IR radiations promotes crystallinity and slightly modifies the relative intensities of peaks. The crystallographic orientation of deposited Ti films changes from the (100) to (002) plane exaltation for 100 W. Inverse trend (from (002) to (100)) is generally observed when changing the DC process to a high power impulse magnetron sputtering (HiPIMS) process [63,64]. Inverse changes found between these papers and our work show that increasing energy impinging onto the substrate by an increase of IR radiation or by an increase of ion energy does not play the same role and does not alter film structure in the same way. At the same time, XRD line broadening remains nearly unaffected, implying negligible changes in average grain size.

On Figure 11c, it is important to note that no oxide phase is detected on these films, whereas a large amount of oxygen is revealed by RBS analyses. It comes that an amorphous TiO_x phase is certainly present in addition to metallic Ti. This is confirmed by the increase of the background signal intensity observed on XRD patterns at low angle diffraction, which can be related to diffusion process by amorphous matter.

Depending on experimental growth conditions, a shift of the angular positions of the (100) and (002) Ti planes, can be noticed. As reference, the (100) and (002) peak positions (dash bars) of bulk α-Ti are given in Figure 11c ; they are located at 35.09° and 38.42°, respectively, and the corresponding “a” and “c” cell parameters are 0.2950 nm and 0.4683 nm (JCPDS # 00-044-1294). The “a” and “c” lattice parameters determined from the (100) and (002) peak positions on the XRD patterns (Figure 11c) are in the ranges 0.2911 – 0.2928 nm and 0.4682 – 0.4704 nm, respectively. Compared to reference values, the “a” parameter is lower while the “c” parameter is higher, meaning that compressive stresses exists in crystallites. In addition, the “c/a” ratios, which range from 1.59 to 1.62 in films, are higher than that of bulk α-Ti (1.587). When increasing power up to 100 W, the positions of the (100) and the (002) are shifted to the corresponding positions of the bulk α-Ti, especially for hot and cold+IR configuration. This means that the 2 cell parameters and the “c/a” ratio become

closer to the ones corresponding bulk α-Ti. Indeed, the "c/a" ratio is slightly inferior to 1.60 for *Ti_Cold_100_IR* and *Ti_Hot_100* thin films.

Thus, it may be concluded from this part that the IR radiations coming from hot target or the IR source have an effect on the structural properties of Ti films. While the *Ti_Cold_50* film is amorphous, *Ti_Hot_50* and *Ti_Cold_50_IR* ones are crystalline and *Ti_Cold_100_IR* and *Ti_Hot_100* exhibit a "c/a" ratio inferior to 1.60 indicating that the presence of IR radiation tends to decrease the compressive stress inside film. Moreover, the crystallographic orientation of deposited Ti films changes form the (100) to (002) plane dominance for 100 W by using hot target configuration inducing IR radiation.

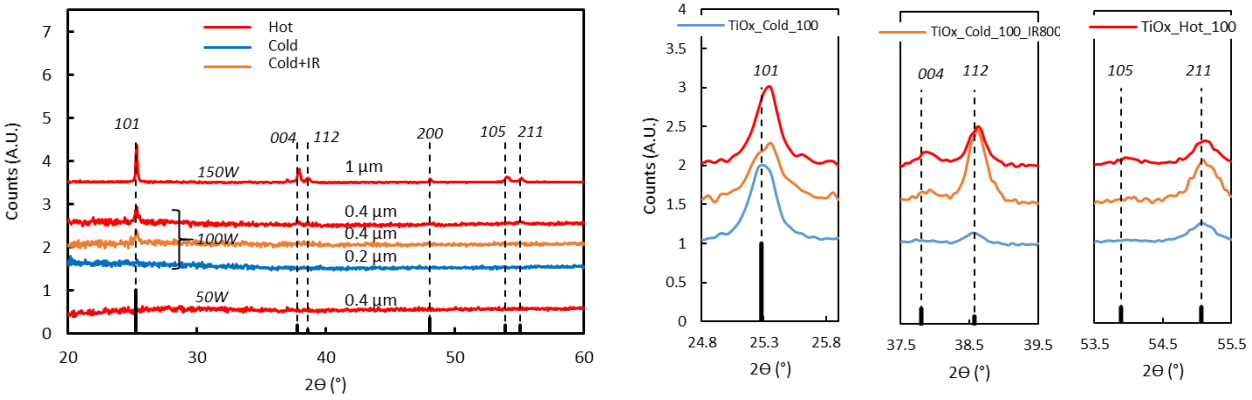

(a) (b)

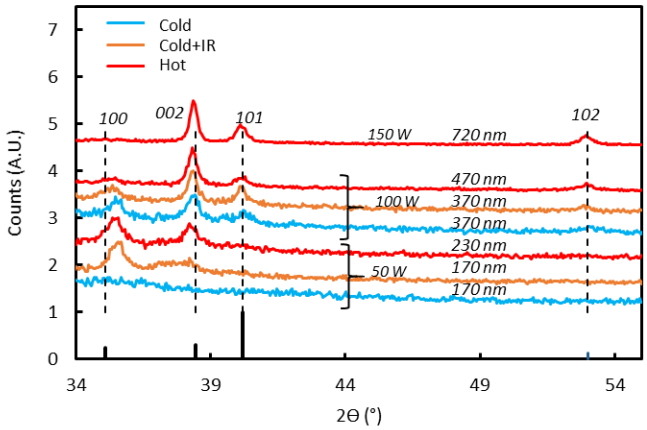

(c)

Figure 11. X-ray diffractograms of (a) TiO_x thin films with various thicknesses, (b) TiOx films with same thickness (1µm) and, (c) Ti thin films in the three configurations: hot (red), cold (blue) and cold with IR radiation (orange). The XRD patterns are compared to JCPDS files corresponding to anatase TiO_2 (# 00-021-1272), and hexagonal α-Ti (# 00-044-1294). No peak related to cubic β-Ti has been found.

4. Conclusion

We have investigated the sputtering of titanium in hot target configuration in pure Ar and in an Ar/O_2 mixture by comparing three configurations: cold target, hot target (insertion of a ceramic disk between the target and the cooled magnetron) and cold target assisted by IR radiations. The effect of target surface temperature (up to about 1000°C) has been evaluated on sputtering process and on properties of Ti, and TiO_x thin films for relatively low power (inferior to 150 W). This study confirms the trends reported in literature: the sputtering of a hot target induces an increase of deposition rate. In the present work, we found a 1.4 factor in metallic mode and a 2 factor in oxide mode for 150 W for which target temperature (measurement and model) reaches about 1000°C. The introduction of O_2 in sputtering apparatus induces an increase of target emissivity and so a slight decrease of temperature.

No evidence of evaporation process, even at the highest temperature, has been found by mass spectrometry. A slight decrease of high energy Ti and Ti^+ species proportion has been detected using spectrometry leading to a decrease of their mean energy when incoming onto the substrate. The influence of the target temperature – especially in reactive (oxygen) sputtering – on the formation of oxygen radicals and negative oxygen ions near the target surface has not been studied but could be of interest. This suggests a modification of the sputtering process efficiency of heated material, leading to a rise of the sputtering yield. This can be related to the binding energy that is known to be lowered at high temperature and may also be the reason for the decrease of the high energy populations of the ejected species. However, this parameter cannot justify alone the deposition rate increase and other ones are probably affected by high temperature. Energy flux measurements have shown that the energy brought by plasma species slightly decreases with the rise of temperature. The important result is that the IR radiation emitted from hot target is the main part (about 80%) of the global energy transferred to the substrate in hot configuration. The influence of this contribution that has been suspected by several authors has clearly been found in the present work to determine final film properties.

All films are found columnar whatever the deposition configuration. Concerning the thin films obtained in Ar/O_2 gas, no clear influence of IR radiation has been obtained on TiO_x thin film microstructure, oxides being slightly denser than metals, as usually reported. The enhancement of oxygen incorporation in thin film is observed in oxide regime from RBS measurement. Working in hot target configuration seems to help synthesizing a nearly-stoichiometric titanium dioxide. This is consistent with an enhancement of the crystalline state of TiO_2 anatase films characterized by crystallites randomly distributed on substrate (even if an

enhancement of the (112) and (211) peaks is observed). Concerning the Ti-based film obtained in pure argon, no oxide phase is detected on these films, whereas a large amount of oxygen is revealed by RBS analyses. It comes that an amorphous TiO_x phase is certainly present in addition to metallic Ti. Raman spectroscopy analysis could have been of interest to precise such microstructure. Hot configuration seems to enhance porosity of Ti-based film only at 150 W and induces columns exhibiting sharp-features. Moreover, crystallinity and crystallographic orientation are slightly improved and modified with a decrease of the compressive stress inside the film.

Finally, the IR radiations emitted in hot target magnetron sputtering are thought to be responsible for the modifications of thin film properties as compared to cold configuration.

Acknowledgements

The first author thanks the "Region Centre Val de Loire" for financial supports during his PhD. The authors thank Thierry SAUVAGE, Olivier WENDLING and Aurélien BELLAMY from the CEMHTI laboratory for RBS measurements on the Pelletron accelerator. All the authors would like to thank S. KONSTANTINIDIS, research associate of the National Fund for Scientific Research (Belgium) and N. SEMMAR, Professor at the University of Orléans, for their useful discussions about energy flux transfer (especially radiative transfer).

References

[1] Donald M. Mattox, Vacuum Evaporation and Vacuum Deposition, chapter 6 in Handbook of Physical Vapor Deposition (PVD) Processing (Second Edition), 2010

[2] P.J. Kelly, R.D. Arnell, Magnetron sputtering: a review of recent developments and applications, Vacuum 56 (2000) 159-172

[3] U. Helmersson , M. Lattemann, J. Bohlmark, A. P. Ehiasarian, J. T. Gudmundsson, Review Ionized physical vapor deposition (IPVD): A review of technology and applications, Thin Solid Films 513 (2006) 1–24

[4] G. Abadias, E. Chason, J. Keckes, M. Sebastiani, G. B. Thompson, E. Barthel, G.L. Doll, C.E. Murray, C.H. Stoessel, L. Martinu, Review Article: Stress in thin films and coatings: Current status, challenges, and prospects, Vac. Sci. Technol. A 36 (2018) 020801

[5] D. Magnfält A. Fillon, R. D. Boyd, U. Helmersson, K. Sarakinos and G. Abadias, Compressive intrinsic stress originates in the grain boundaries of dense refractory polycrystalline thin films, J. of Appl. Phys. 119 (2016) 055305

[6] F. Spaepen, Interfaces and stresses in thin film, Acta Materialia 48 (2000) 31-42

[7] J.A. Thornton, Influence of apparatus geometry and deposition conditions on the structure and topography of thick sputtered coatings, J. Vac. Sci. Technol. 11 (1974) 666

[8] A. Anders, A structure zone diagram including plasma-based deposition and ion etching, Thin Solid Films 518 (2010) 4087

[9] H. Kersten, H. Deutsch, H. Steffen, G.M.W. Kroesen, R. Hippler, The energy balance at substrate surfaces during plasma processing, Vacuum 63 (2001) 385

[10] S Bornholdt, N Itagaki, K Kuwahara, H Wulff, M Shiratani and H Kersten, Characterization of the energy flux toward the substrate during magnetron sputter deposition of ZnO thin films, Plasma Sources Sci. Technol. 22 (2013) 025019

[11] D.M. Mattox, Particle bombardment effects on thin-film deposition: A review, Journal of Vacuum Science & Technology A 7 (1989) 1105

[12] I. Petrov, F. Adibi, J. E. Greene, L. Hultman, and J.-E. Sundgren, Average energy deposited per atom: A universal parameter for describing ion assisted film growth, Appl. Phys. Lett. 63 (1993) 36

[13] K. Sarakinos, J. Alami, S. Konstantinidis, High power pulsed magnetron sputtering: A review on scientific and engineering state of the art, Surf. and Coat. Technol.204 (2010) 1661–1684

[14] P.-A. Cormier, A. Balhamri, A.-L. Thomann, R. Dussart, N. Semmar et al. Measuring the energy flux at the substrate position during magnetron sputter deposition processes, J. Appl. Phys. 113 (2013) 013305

[15] T. Kubart, D. Depla, D. M. Martin, T. Nyberg, and S. Berg, High rate reactive magnetron sputter deposition of titanium oxide, Appl. Phys. Lett. 92 (2018) 221501.

[16] H. Toku, R.S. Pessoa, H.S. Maciel, M. Massi, U.A. Mengui, The effect of oxygen concentration on the low temperature deposition of TiO_2 thin films, Surf. and Coat. Technol.202 (2008) 2126–2131

[17] J. Musil, D. Heman, and J. Šícha, Low-temperature sputtering of crystalline TiO_2 films, J. of Vac. Sci. & Technol. A 24 (2006) 521

[18] D. Rohde, P. Pecher , H. Kersten , W. Jacob , R. Hippler, The energy influx during plasma deposition of amorphous hydrogenated carbon films, Surf. and Coat. Technol.149 (2002) 206–216

[19] *J*. Musil, V. Satava, P. Baroch, High-rate reactive deposition of transparent SiO_2 films containing low amount of Zr from molten magnetron target, Thin Solid Film 519 (2010) 775-777

[20] W. F. Yang, Z. G. Liu, Z. Y. Wu, M. H. Hong, C. F. Wang, Alex Y. S. Lee, and H. Gong, Low substrate temperature fabrication of high-performance metal oxide thin-film by magnetron sputtering with target self-heating, Appl. Phys. Lett. 102 (2013) 111901

[21] A. E. Lapshin, V. S. Levitskii, V. I. Shapovalov, A. E. Komlev, E. S. Shutova, I. L. Mylnikov, and A. A. Komlev, Composition and Structure of Copper Oxide Films Synthesized by Reactive Magnetron Sputtering with a Hot Target, Glass Physics and Chemistry 42 (2016) 359–362

[22] A.M. Ismailov, V. A. Nikitenko, M. R. Rabadanov, L. L. Emiraslanova, I. Sh. Aliev, M. Kh. Rabadanov, Sputtering of a hot ceramic target: Experiments with ZnO, Vacuum 168 (2019) 10885

[23] M. Laurikaitis ,J. Cyviene , J. Dudonis, Deposition of Zr–ZrOX and Y–YXOY films by reactive magnetron sputtering, Vacuum 78 (2005) 395–399

[24] D. V. Sidelev, G. A. Bleykher, V. P. Krivobokov, Z. Koishybayeva, High-rate magnetron sputtering with hot target, Surf. Coat. Technol. 308 (2016) 168-173

[25] D.V. Sidelev, G.A. Bleykher, M. Bestetti, V.P. Krivobokov, A. Vicenzo, S. Franz, M.F. Brunell, A comparative study on the properties of chromium coatings deposited by magnetron sputtering with hot and cooled target, Vacuum 143 (2017) 479-485

[26] V. A. Grudinin, G. A. Bleykher, D. V. Sidelev, V.P. Krivobokov, M. Bestetti, A. Vicenzo, S. Franz, Chromium films deposition by hot target high power pulsed magnetron sputtering: Deposition conditions and film properties, Surf. and Coat. Technol.375 (2019) 352–362

[27] K. Kawamata, T. Shouzu and N. Mitamura, K-M-S (keep-molecules sputtering) deposition of optical MgF2 thin films, Vacuum 51 (1998) 559-564

[28] D. Mercs, F. Perry, A. Billard, Hot target sputtering: A new way for high-rate deposition of stoichiometric ceramic films, Surf. and Coat. Technol.201 (2006) 2276

[29] Hyun Jung Kim, High mobility $Si_{0.15}Ge_{0.85}$ growth by using the molten target sputtering (MtS) within heteroepitaxy framework, Scientific Reports (2019) 9:11555

[30] A. Caillard, M. El'mokh, T. Lecas, A.−L. Thomann., Effect of the target temperature during magnetron sputtering of Nickel, Vacuum 147 (2018) 82

[31] D. V. Sidelev, G. A. Bleykher, V. A. Grudinin, V.P. Krivobokov, M. Bestetti, M. S. Syrtanov, E. V. Erofeev, Hot target magnetron sputtering for ferromagnetic films deposition, Surf. and Coat. Technol. 334 (2018) 61-70

[32] D. V. Sidelev, V. P. Krivobokov, Angular thickness distribution and target utilization for hot Ni target magnetron sputtering, Vacuum 160 (2019) 418–42

[33] V.A. Gerasimov, D.K. Kostrin, L.M. Selivanov, A.A. Uhov, A.E. Komle, E.S. Shutova, Method of magnetron target temperature evaluation by analysis of thermal radiation spectrum, J. Phys.: Confer. Series. 729 (2016) 012019

[34] V. I. Shapovalov, E. A. Minzhulina, Studying heating of magnetron target based on measurement of substrate temperature, Vacuum 161 (2019) 324-327

[35] V.V. Karzin, A.E. Komlev, K.I. Karapets, N.K. Lebedev, Simulation of heating of the target during high-power impulse magnetron sputtering, Surf. and Coat. Technol.334 (2018) 269–273

[36] G.A. Bleykher, V.P. Krivobokov, A.V. Yuryeva, Magnetron deposition of coatings with evaporation of the target, Techn. Phys. 60 (2015) 1790–1795

[37] G.A. Bleykher, V.P. Krivobokov, A.V. Yurjeva, I. Sadykova, Energy and substance transfer in magnetron sputtering systems with liquid-phase target, Vacuum 124, 11 (2016) 11-17

[38] G.A. Bleykher, A.O. Borduleva, V.P. Krivobokov, D.V. Sidelev, Evaporation factor in productivity increase of hot target magnetron sputtering systems, Vacuum 132 (2016) 62-69

[39] P.-A.Cormier, A.-L.Thomann, V.Dolique, A.Balhamric, R.Dussart, N.Semmar, T.Lecas, P.Brault, R.Snyders, S.Konstantinidis, IR emission from the target during plasma magnetron sputter deposition, Thin Solid Films 545 (2013) 44-49

[40] A.A. Kozin, V. I. Shapovalov, Modeling of thermal processes in magnetrons with single hot target and “sandwich-target”, Surf. and Coat. Technol. 359 (2019) 451

[41] V.I. Shapovalov, Hot Target. Physicochemical Model of Reactive Sputtering, Techn. Phys. 64 (2019) 926-932

[42] J. Tesař , J. Martan, J. Rezek, On surface temperatures during high power pulsed magnetron sputtering using a hot target, Surf. and Coat. Technol.206 (2011) 1155

[43] I. Setién-Fernández, T. Echániz, L. González-Fernández, R.B. Pérez-Sáez, M.J. Tello, Spectral emissivity of copper and nickel in the mid-infrared range between 250 and 900 °C, International Journal of Heat and Mass Transfer 71 (2014) 549–554

[44] Y.S. Touloukian and D.P. DeWitt, Thermophysical Properties of Matter, Vol. 7: Thermal Radiative Properties, IFI/Plenum, New York, 197

[45] A.-L. Thomann, N. Semmar, R. Dussart, and J. Mathias, Diagnostic system for plasma/surface energy transfer characterization, Rev. Sci. Instrum. 77 (2006) 033501

[46] M.F. Modest, Radiative Heat Transfer, McGraw-Hill, New York, 1993

[47] E Amin-Chalhoub, N Semmar, L Coudron, G Gautier, C Boulmer-Leborgne, A Petit, M Gaillard, J Mathias and E Millon, Thermal conductivity measurement of porous silicon by the pulsed-photothermal method, J. Phys. D: Appl. Phys. 44 (2011) 355401

[48] E. Amin-Chalhoub, G. Wattieaux, N. Semmar, M. Gaillard, A. Petit, and C. Leborgne, Improvement of the identification of multiwall carbon nanotubes carpet thermal conductivity by pulsed photothermal method, J. Appl. Phys. 112 (2012) 094322

[49] A. Melhem, D. De Sousa Meneses, C. Andreazza-Vignolle T. Defforge, G. Gautier, A. Sauldubois, N. Semmar, Structural, Optical, and Thermophysical Properties of Mesoporous Silicon Layers: Influence of Substrate Characteristics, J. Phys. Chem. C2017, 121, 7821−7828

[50] E.M. Sparrow, Radiative Heat Transfer, 1978

[51] A. Anders, J. Andersson, and A. Ehiasarian, High power impulse magnetron sputtering: Current-voltage-time characteristics indicate the onset of sustained self-sputtering, J. of Appl. Phys. 102, (2007) 113303

[52] V.V. Gvozdev, M.A. Kurzanov, A.M. Marahtanov, Plasma Phys. Rep. 5 (1999) 488-492

[53] T. E. Sheridan and J. Goree, Collisional plasma sheath model, Physics of Fluids B: Plasma Physics 3, (1991) 2796

[54] J. M. Blocher, and I. E. Campbell, Vapor Pressure of Titanium, J. of the Amer. Chem. Soc. 71 (1949) 4040

[55] S. Dushman, Scientific Foundations of Vacuum Technique. New York-London, John Wiley and Sons Inc., 1962, p. 614

[56] M. Stepanova and S. Dew, Anisotropic energies of sputtered atoms under oblique ion incidence, Nuclear Instruments and Methods in Physics Research Section B: Beam Interactions with Materials and Atoms 215 (2004) 357–365

[57] A.-L. Thomann, A. Caillard, M. Razaa, M. El'Mokh, P.A.Cormier, S.Konstantinidis, Energy flux measurements during magnetron sputter deposition processes, Surf. and Coat. Technol. 377 (2019) 124887

[58] Edward D. Palik, Handbook of optical constant and solids, pp. 283-286

[59] I. Petrov, P. B. Barna, L. Hultman, and J. E. Greene, Microstructural evolution during film growth, J. of Vacuum Sci. & Technol. A 21 (2003) S117

[60] P.B. Barna, M. Adamik, Fundamental structure forming phenomena of polycrystalline films and the structure zone models, Thin Solid Films 317 (1998) 27

[61] S. Mahieu, P. Ghekiere, D. Depla, R. De Gryse, Biaxial alignment in sputter deposited thin films, Thin Solid Films 515 (2006) 1229–1249

[62] S. Mráz and J. M. Schneider, Structure evolution of magnetron sputtered TiO_2 thin films, J. of Appl. Phys. 109 (2011) 023512

[63] F. J. Jing, T. L. Yin, K. Yukimura, H. Sun, Y. X. Leng, and N. Huang, Titanium film deposition by high-power impulse magnetron sputtering: Influence of pulse duration, Vacuum 86 (2012) 2114

[64] N. Britun,1 M. Michiels, T. Godfroid, and R. Snyders, Ion density evolution in a high-power sputtering discharge with bipolar pulsing, Appl. Phys. Lett. 112 (2018) 234103